Electrochemical Properties of Iron Oxide Decorated Activated Carbon Cloth as a Binder-Free Flexible Electrode

M. G. C. Munhoz[a]* ⓘ *, A. C. Rodrigues-Siqueli[b]* ⓘ *, B. C. S. Fonseca[b]* ⓘ *, J. S. Marcuzzo[c]* ⓘ *,*

J. T. Matsushima[d], G. F. B. Lenz e Silva[a] ⓘ *, M. R. Baldan[b], G. Amaral-Labat[b]* ⓘ

[a]Universidade de São Paulo, Departamento de Engenharia Metalúrgica e de Materiais, Avenida Mello Moraes, 2463, Cidade Universitária, 05508-030, São Paulo, SP, Brasil.
[b]Instituto Nacional de Pesquisas Espaciais, Av. dos Astronautas, 1758, Jardim da Granja, 12227-010, São José dos Campos, SP, Brasil.
[c]JMHP - Consultoria em Materiais e Informática Ltda, Rua Glauber Rocha, 187, 12301-600, Jacareí, SP, Brasil.
[d]Faculdade de Tecnologia de São José dos Campos - Professor Jessen Vidal, Avenida Cesare Monsueto Giulio Lattes, 1350, Distrito Eugênio de Melo, 12247-014, São José dos Campos, SP, Brasil.

The oxidation and deposition of transition metal oxides on porous carbon precursor materials strongly influence the final performance of supercapacitor electrodes. Thus, the influence of oxidation time combined with simple iron oxide deposition was evaluated on a flexible carbon fiber cloth electrode oxidized at three different times and exposed to spontaneous iron oxide deposition. The 140 minutes oxidation time increased by two times the iron quantity deposited on the activated carbon fiber cloth (ACC) and also increased the crystallinity of the carbon matrix. The iron oxide deposition improved the contribution of anions to store energy, enhancing the pseudocapacitive effect in the samples. The optimal oxidation time of the ACC140_Fe sample with the greater iron oxide deposition achieves 116.8 F g^{-1}. The binder-free flexible electrode presents a successful design through pre-oxidation and spontaneous iron oxide deposition on the carbon matrix without expensive and environmentally unfriendly chemical treatments.

Keywords: *Energy storage, Flexible electrodes, Supercapacitors, Spontaneous deposition, Oxidation.*

1. Introduction

The high demand for energy storage is changing how we buy, sell, and use energy. The development of storage technologies for new portable electronic devices, wearables, and electric vehicles is linked to the research of new electrode materials with fast charging, high energy outputs, and long lifetime[1,2]. Conventional batteries and capacitors are not satisfactory enough for new devices systems, which simultaneously require high power and high energy densities[2-4]. Thus, supercapacitors emerge to fulfill this gap. They have been developed from several materials, such as carbon-based materials, spinel ferrites, perovskite oxides, transition metals sulfides, and conducting polymers[5].

Porous carbon materials such as activated carbon[6], CNT[7], graphene oxide (GO)[8], reduced GO (rGO)[9], xerogel-like[10], and aerogels[11] are largely applied for supercapacitor electrodes because of properties like high surface area, chemical stability, high conductivity, and stable electrochemical properties[1,2,12]. Activated carbon fibers are attractive materials for supercapacitor electrodes or other applications[13], especially because of their flexible structure and three-dimensional arrangement comprising a continuous

current path, decreasing the interparticle resistance[2,14] and increasing the surface area simultaneously. Consequently, a large number of charges is able to be stored in the electrical double layer[15]. Such morphology simplifies the electrode assembly preparation and avoids the use of binders, which are required for powder materials[16]. Binders are high-priced compared to the active material from the electrode and are responsible for increasing the electrical resistivity and the total cost, reducing the final performance of the device. The use of low-cost polyacrylonitrile (PAN) textile precursor might be a good strategy to overcome these issues and avoid the use of raw materials for aeronautical carbon fiber[13,17]. Besides, PAN textile already presents nitrogen groups in their chemical structure, assisting in the pseudocapacitive reactions[18].

Several treatments on the carbon surface can be explored to increase the electrochemical performances of the carbonaceous matrix[19-23]. The introduction of heteroatoms on the carbon surface, such as nitrogen, oxygen, sulfur, and phosphorus, generally affects properties like wettability and conductivity[24], changing the total capacitance. A thermal oxidation process is a simple approach used to change the surface chemistry by the formation of oxygenated functional

groups on the carbonaceous matrix-like carbon fibers, even before the carbonization and/or activation processes[18]. The greater amount of oxygenated functional groups was correlated to larger capacitance values[25-27]. Besides, grafted transitional metal oxides are widely used with carbon, providing great electrochemical performances[12,28,29] through a redox contribution to the total capacitance, usually called pseudocapacitance[30]. This faradaic contribution to the energy storage might be easily obtained with the addition of metallic oxides, such as Zn, Co, Ti, Fe, Ag, and Mn[31-33] in the carbon matrix. Among these, iron oxides have advantages such as low cost, environmental friendliness, abundant availability, and non-toxicity[34].

The total capacitance of an electrochemical device is affected by the double-layer storage and faradaic reactions contributions. In general, cations and anions involved in energy storage might present different contributions to the formation of the double layer charges and the pseudo-capacitive reactions[35]. Such ions allow a balance of the negative and positive charges, typical of hybrid supercapacitors. Thus, the contributions associated with the ion might provide important information about the electrolyte-electrode interface. Despite this, only a few research explore the contribution of cations and anions in the total capacitance[36-39].

This work evaluates binder-free flexible cloth from PAN textile as electrodes for supercapacitors. The fibers were thermally oxidized, CO_2 activated, and then submitted to a spontaneous deposition of iron oxide performed in the final activated carbon cloth (ACC). The contribution of ions in acidic aqueous electrolyte (H_2SO_4 2 mol L^{-1}) was investigated for application as electrodes for supercapacitors without laborious and expensive binders, reaching capacitances values up to 116.8 F g^{-1}.

2. Experimental

All carbon materials were prepared with textile PAN fibers. First, PAN textile was converted to ACC through thermal oxidation at 250 °C using three different times: 110, 140, and 170 minutes. Then, it was carbonized under an argon atmosphere at 900 °C for 20 minutes and activated at 1000 °C for 2 hours under carbon dioxide. The spontaneous iron deposition on the ACC was carried out using a 2.88 g L^{-1} $Fe(NO_3)_3$ aqueous solution, where the samples of ACC were immersed into the solution for 24 hours at room temperature[40]. After the adsorption step, the samples were washed with deionized water, dried in a vacuum oven at 50 °C for 24 hours, and labeled according to the oxidation time of each sample (ACC110_Fe, ACC140_Fe, and ACC170_Fe).

The microstructure of flexible electrodes was analyzed through Field Emission Gun Scanning Electron Microscopy (FEG-SEM), TESCAN model MIRA3 equipped with energy-dispersive X-ray spectroscopy (EDX), Oxford X-MAX detector. The Raman spectra were recorded using a Horiba Scientific model Labram Hr Evolution spectrometer (514.6 nm). The spectra deconvolution was performed by the method reported by Sadezky[41]. The X-Ray Diffractometry (XRD) was performed in a PANalytical X'PertPRO diffractometer using CuKα (λ=1.54 Å) radiation.

The surface groups characterization was performed using an X-ray photoelectron spectroscopy (XPS) Kratos

Axis Ultra with a monochromatic Al-Kα (1486.5 eV). The vacuum was stabilized at 10^{-7} Pa, and the scans were performed with 40 eV pass energy and a step size of 1 eV. The binding energy of all samples was calibrated to carbon, C 1s peak at 285 eV, of adventitious carbon[42,43]. The results were evaluated with CASA XPS software. The pore textural of samples was characterized with a Micromeritics ASAP 2020 Plus instrument by N_2 adsorption/desorption isotherms at 77 K. The specific surface area (S_{BET}) and the total volume of micropores, pore size <2 nm (V_{DR}), were calculated using the Brunauer–Emmett–Teller[44] and Dubinin–Raduskevich[45] methods, respectively. The total pore volume ($V_{0.97}$) was deduced from the amounts of nitrogen adsorbed at $P/P_0 = 0.97$, and the volume of mesopores (V_{meso}) was estimated by the difference between the total pore volume and the volume of micropores ($V_{0.97} - V_{DR}$).

Electrochemical measurements were performed in a three-electrode cell using a PGSTAT 302N Autolab potenciostatic/galvanostatic. ACC was cut with a steel hole punch into 5 mm diameter circular samples and used as working electrodes. The counter electrode was a platinum plate, and the reference electrode was Ag/AgCl in an aqueous electrolyte solution (H_2SO_4 2 M) at room temperature.

3. Results and Discussion

3.1. Morphological and textural properties

All the electrodes presented a high ability to bend (Figure 1a), enabling their use in flexible devices[1,16,44,46,47]. The morphology of all flexible electrodes was observed with a FEG-SEM (Figure 1b-e). The ACC presents typical grooves from the fiber manufacture (Figure 1b-d), and iron oxide microparticle precipitates distributed on the fibers (blue arrows) (Figure 1b-d), as confirmed by EDX analysis (Figure 1e).

Elemental mapping by energy dispersive X-ray spectrometry (Figure 2) was performed for all the samples. As expected, carbon, oxygen, and nitrogen species from the fiber chemical composition are found on the material surface. Additionally, micro- and nano-particles of iron are homogeneously distributed on the carbonaceous matrix. Interestingly, microparticles of the iron match with oxygen, suggesting the formation of iron oxide.

Table 1 shows the textural properties of the ACC electrodes. Interestingly, the surface area increased with the oxidation time, reaching a maximum of 624 m² g⁻¹ for the ACC170_Fe. Therefore, the thermal oxidation process is correlated with increased porosity[18]. Furthermore, the fibers present large quantities of micropores (0.16 – 0.24 cm³ g⁻¹), and such textural porosity is aimed for application in electrodes for supercapacitors[25,48].

Table 1. Textural properties of carbon electrodes.

Electrodes	S_{BET} $(m^2\ g^{-1})$	$V_{0.97}$ $(cm^3\ g^{-1})$	V_{DR} $(cm^3\ g^{-1})$	V_{meso} $(cm^3\ g^{-1})$
ACC110_Fe	440	0.17	0.16	0.01
ACC140_Fe	557	0.22	0.22	0
ACC170_Fe	624	0.24	0.24	0

The N$_2$ isotherms (Figure 3a) are type I for all samples[49], typical of microporous materials. The curves agree with the mesopores and micropores volume calculated, i.e., the materials are exclusively microporous. The pore size distributions show a peak pore centered at 0.72 nm for all samples (Figure 3b).

3.2. Chemical and structural composition

Spectra and elemental analysis of the samples evaluated through XPS are presented in Figure 4. The electrodes showed the presence of carbon, oxygen, and nitrogen from the carbon matrix precursor and iron oxide from the spontaneous deposition, as expected. The highest amount of iron in the oxidized sample surface is presented in the sample ACC140_Fe (4.08%). This value is twice the amount of iron deposited on activated carbon cloth with oxidation of 50 minutes (2.1%)[40]. Those findings suggest that an oxidation time of 140 minutes is optimal for iron oxide deposition.

The N/C, O/C, and Fe/C ratios (Table 2) were calculated from the elemental analysis. A reduction of carbon amount is compensated for the increase in iron, nitrogen, and oxygen content, probably associated with the increase of heteroatoms on the carbon matrix.

The oxidation step of the carbonaceous matrix had a strong influence on the chemical surface characteristics, acting mainly in the formation of different nitrogenated and oxygenated functional groups. Consequently, it has a significant influence on the faradaic reactions of the final electrode[18]. The oxygenated and nitrogenated groups presented in the ACC140_Fe electrode might provide active sites for pseudocapacitive reactions[18,25]. Normally, higher oxidation times of PAN fibers generate surface groups such as C–O, C–OH, C–O–C, and reduce adsorbed water[35]. Therefore, the additional oxidation performed on the electrodes probably
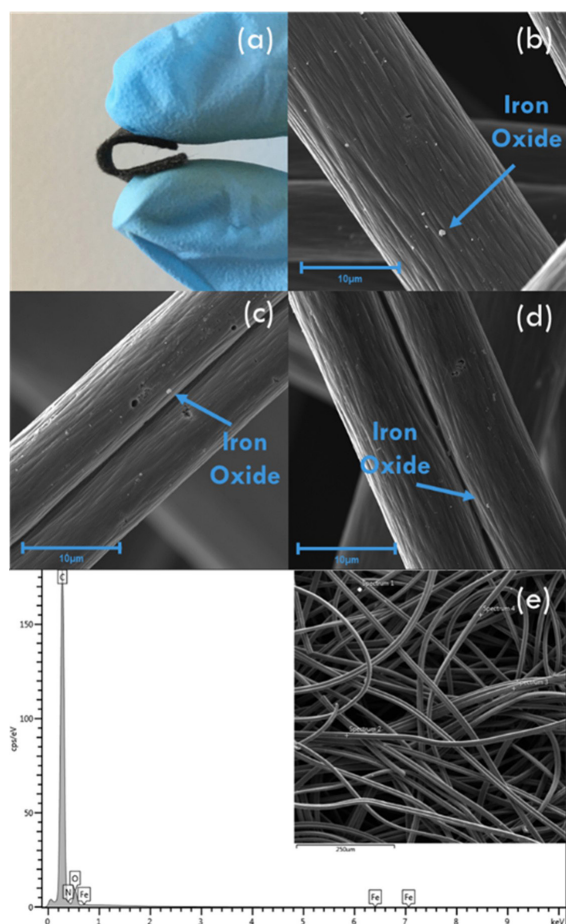

Figure 1. (a) Flexible electrode ACC140_Fe. FEG-SEM (b) ACC110_Fe; (c) ACC140_Fe; (d) ACC170_Fe; (e) EDX spectra of ACC140_Fe.

Table 2. N/C, O/C, and Fe/C ratios calculated for the samples.

SAMPLES	N/C (%)	O/C (%)	Fe/C (%)
ACC110_Fe	1.93	17.09	0.91
ACC140_Fe	2.06	29.03	5.58
ACC170_Fe	2.41	21.29	2.34

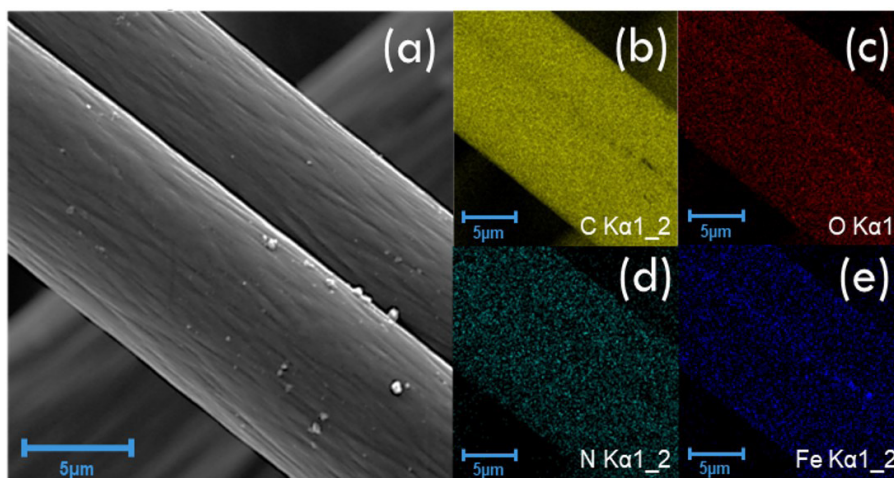**Figure 2.** SEM image of (a) ACC140_Fe and its respective elemental mapping of (b) carbon (C); (c) oxygen (O); (d) nitrogen (N), and (e) Iron (Fe).
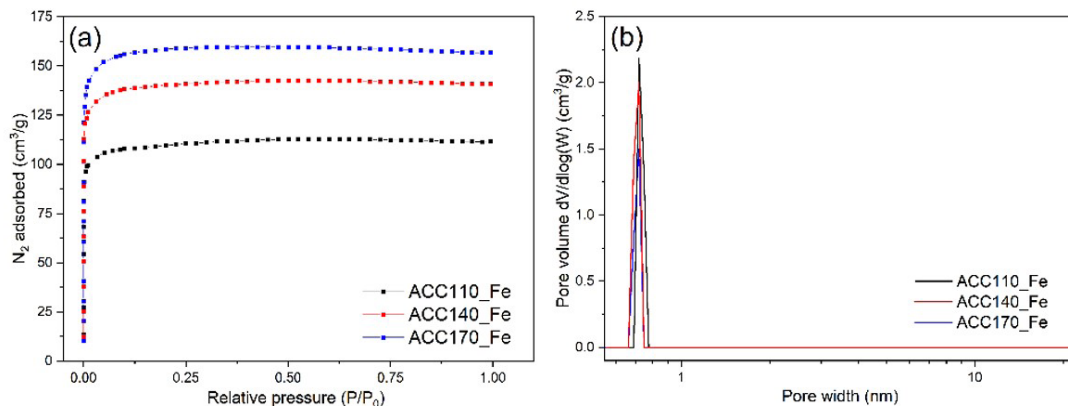
Figure 3. (a) N_2 isotherms at 77 K of ACC electrodes and (b) pore size distribution calculated from DFT model.
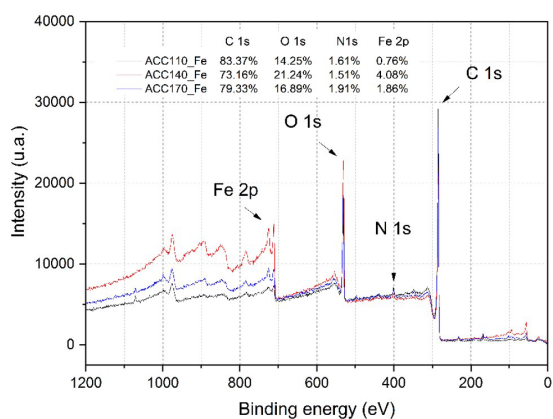

Figure 4. XPS survey spectra of the samples ACC110_Fe, ACC140_Fe, and ACC170_Fe.

produced a higher number of oxygenated groups, which might be associated with iron species.

The high-resolution O 1s spectra, Figure 5, presented carbonyl groups (C=O 531 eV), ether groups (C-O 532.3 eV), and hydroxyl groups/chemisorbed water (C-OH 533.5 eV)[50].

The deconvolution of Fe 2p spectra is seen in Figure 6. The figure shows the main peaks of $Fe^{3+}_{3/2}$ and $Fe^{3+}_{1/2}$ at 711.6 and 725.6 eV, respectively. The spin-orbit splitting (BE $2p_{1/2}$-$2p_{3/2}$) of 13,4 eV was obtained, and peaks were identified from deconvolution[51].

The Fe 2p high-resolution spectra presented a complex shape, showing multiple states of division because of electron exchange interactions. The produced multiplets are normally reported for α,γ-Fe_2O_3 and α,γ-FeOOH species[40,50]. Furthermore, the associated satellite peaks between 719.2 and 719.6 eV found in the ACC140_Fe are characteristic of the Fe^{3+} species, typically seen in Fe_2O_3[52,53], corroborating the chemical phase found in the elemental mapping.

Complementary information about the chemical structure of electrodes was evaluated by XRD and RAMAN analysis. Figure 7 shows the XRD characterization of the samples. Except for ACC140_Fe, crystallinity decreases with increasing

oxidation time, suggesting that there is an addition of oxygenated groups in the carbon matrix, as already corroborated by XPS analysis. The diffractograms showed carbon peaks around 25° and 45° related to the crystallographic planes of graphite (002) and (100), respectively[53]. However, iron was not found in the evaluated samples, probably due to non-crystalline species deposited on the electrodes.

On the other hand, the Raman spectra presented peaks centered at 1350 cm^{-1} and 1600 cm^{-1}, respectively as D and G bands, Figure 8a. Those bands are characteristic of carbon materials, and their deconvolutions were performed to evaluate the type of structural defects of the studied samples, Figure 8b. The deconvolution method reported by Sadezky[41] was used to adjust those bands.

The D band is related to defects in the graphitic structure, while the G band is associated with the elongation of the C-C bond of the sp^2 atom pairs, characteristic of carbonaceous materials[41]. The deconvolution of the Raman displacement (Figure 8b) also allowed calculating the I_D/I_G ratio for all the samples. Usually, the I_D/I_G ratio is a parameter used to analyze the increase in defects in the graphical structure as an indicator of disorder[54]. All samples presented a high degree of disorder. Nonetheless, the ACC140_Fe electrode showed a smaller disordered structure compared to ACC110_Fe and ACC170_Fe, in agreement with previous XRD results.

3.3. Electrochemical characterization

The electrochemical measurements were performed for all iron-deposited samples, and the total cyclic voltammogram (CV), as well as the cations and anions CVs, in the acid electrolyte (H_2SO_4 2 M) are presented in Figure 9.

As explained elsewhere[48,55], in an aqueous solution, the sulfuric acid dissociates in two dominant ions: bisulfate (HSO_4^-) and hydronium (H_3O^+). The open-circuit potential (OCP) is the point that separates those contributions[36]. After OCP estimation, the ions contribution was separated for each electrode system.

Figure 9 shows the total potential window, comprising the cathodic and anodic responses for all electrodes. A slight increase in intensity at very negative potentials and very positive potentials is associated with water electrolysis,
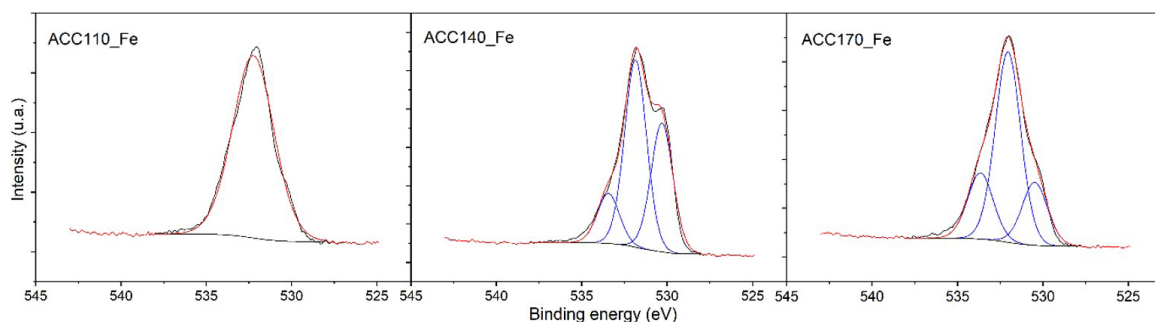
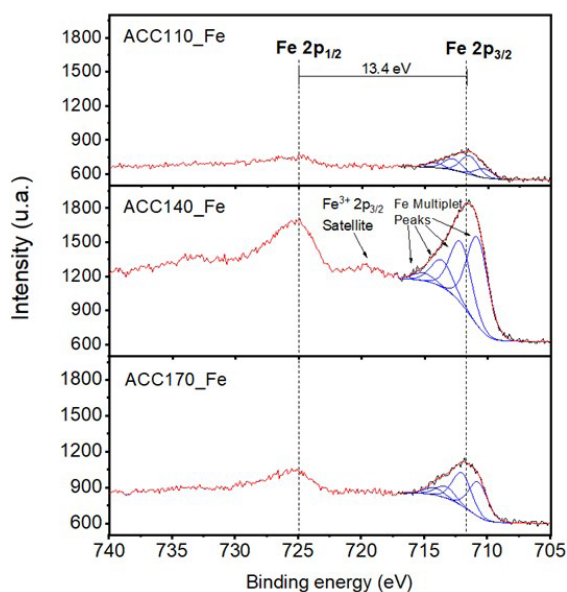**Figure 5.** Deconvoluted XPS O 1s spectra to ACC110_Fe, ACC140_Fe, and ACC170_Fe.

Figure 6. Deconvoluted XPS Fe 2p spectra to ACC110_Fe, ACC140_Fe, and ACC170_Fe.
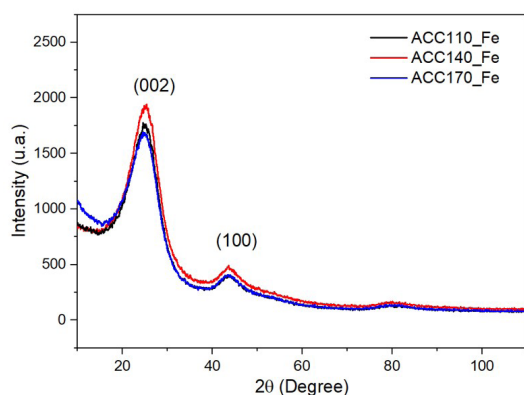

Figure 7. XRD diffractogram ACC110_Fe, ACC140_Fe, and ACC170_Fe.

based on the evolution of hydrogen (negative potentials) and oxygen (positive potentials). Cation-associated CVs (H_3O^+) show rectangular shapes characteristic of double-layer capacitance, while anion-associated CVs (HSO_4^-) show mixed behavior curves involving pseudocapacitance and double-layer capacitance[36]. The CVs also show that samples with greater current density amplitude, ACC140_Fe, and ACC170_Fe, have elevated surface area (S_{BET}) and total pore volume ($V_{0.97}$), exclusively composed of micropores (V_{DR}) with diameters lesser than 2 nm (Table 1 and Figure 3b).

The galvanostatic charge/discharge curves (GCDC) were obtained from electrochemical measurements for all samples. The total potential window of ACC140_Fe is seen in Figure 10a, comprising the cathodic and anodic responses shown in Figures 10b and 10c, respectively. The specific capacitances associated with cations and anions, measured in the range of the cathodic and the anodic potentials, were determined from galvanostatic measurements performed at 1 mA.

The triangular shape of the curves is characteristic of materials with a predominance of electrical double-layer capacitive (EDLC) effects. At the same time, the lack of linearity of the curve indicates the reversible redox reaction (pseudo-capacitive reactions), typical for carbon with quinone/hydroquinone (C=O) groups, corresponding to the anodic and cathodic peaks at 0.38-0.4 V vs. Ag/AgCl found in the voltammograms[37]. Those pseudocapacitive reactions are probably related to the presence of iron and oxygen groups on the carbon matrix surface, as shown through XPS analysis.

The total specific capacitance, measured in the full potential window, and the specific capacitance associated with cations and anions, measured in the cathodic and anodic potential range, respectively, were determined from galvanostatic measurements at 1 mA in a potential window from 0 to 1 V according to:

$$C = \frac{I.t}{\Delta V.m} \qquad (1)$$

where I is the applied current; t is the time for discharge, ΔV is the potential range, and m is the weight of the samples. Table 3 summarizes the total specific capacitance, the cationic, and the anionic capacitances obtained with Equation 1.

The ACC140_Fe electrode presented the highest density amplitude and the highest capacitance value, 116.8 F g^{-1} (Figure 10a). Interestingly, the ACC170_Fe sample presented a lower capacitance value than ACC140_Fe, despite the highest surface area of such material, indicating that the presence of heteroatoms, especially iron and oxygen, on the matrix was essential to increase the electrochemical performance.
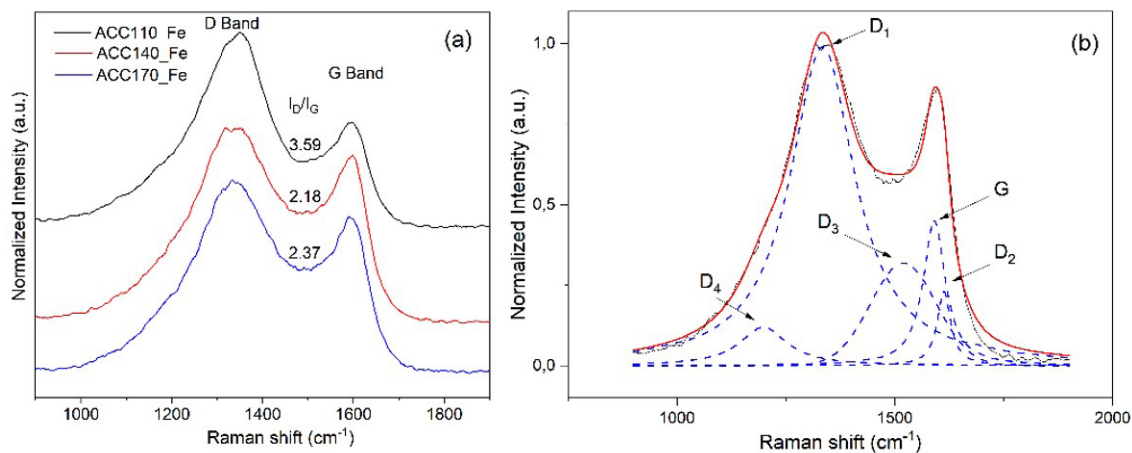
Figure 8. (a) Raman spectra of ACC110_Fe, ACC140_Fe, and ACC170_Fe samples and (b) adjustment of the Raman spectra of the sample ACC140_Fe.
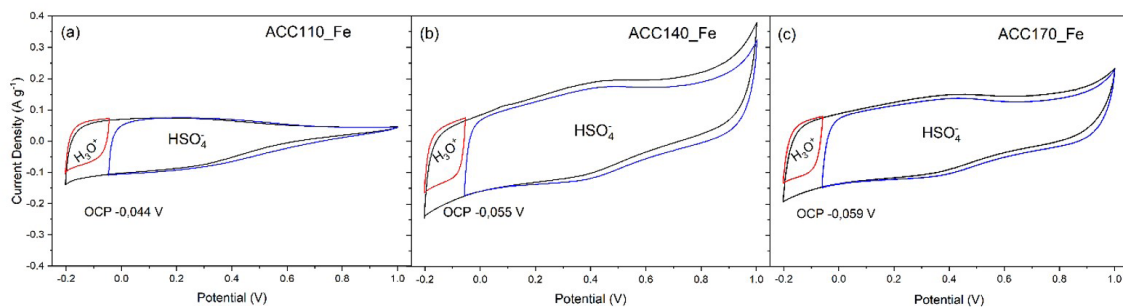

Figure 9. Cyclic voltammetry of samples (a) ACC110_Fe, (b) ACC140_Fe, and (c) ACC170_Fe in aqueous solution H_2SO_4 2 mol L^{-1}.
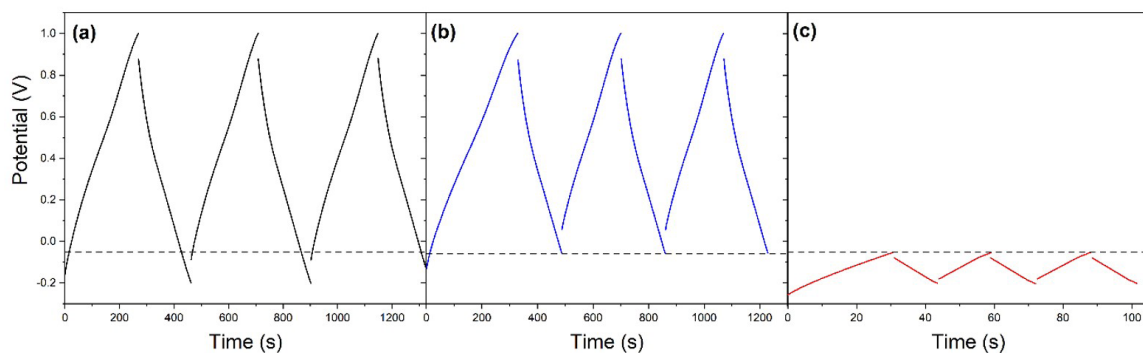

Figure 10. GCDC performed at 1 mA of ACC140_Fe sample: (a) total potential window -0.2 at 1 V; cathodic potential range (before the OCP) and (c) anodic potential range (after the OCP).

Table 3. Calculated capacitance values of ACC electrodes.

SAMPLES	Cs (F g^{-1})	C_ (F g^{-1})	C$_+$ (F g^{-1})
ACC110_Fe	71.9	63.9	10.1
ACC140_Fe	116.8	110.4	4.2
ACC170_Fe	97.3	91.7	1.2

It is clear that the capacitance obtained for ACC electrodes results in extremely high anion adsorption. The anion capacitance is more than six times higher than the capacitance for cation adsorption. Despite the relation between the specific capacitances and the same intensities of anodic and cathodic peaks, the high values of anions specific capacitance are associated with the electrochemical intercalation phenomenon of anions due to the remaining graphitic structure[37]. The samples ACC140_Fe and ACC170_Fe have greater anion specific capacitance, and consequently greater anion intercalation, pointing out samples with greater graphitic structure in agreement with XRD and Raman results.

Nyquist plots of the electrodes are presented in Figure 11. The equivalent series resistance (ESR) and charge transfer resistance (R_{ct}) were estimated from the total equivalent circuit using the curve fitting of the electrochemical impedance spectroscopy (EIS) plot. All the samples present a semicircle in the high-frequency region associated with the charge transfer at the interface between the electrode and the electrolyte[8]. Additionally, the vertical shape of electrodes produced at 140 and 170 minutes at a low-frequency range is attributed to the EDLC characteristic of the ions diffusion process on porous structure[56].

As seen in Table 4, the ACC140_Fe electrode presented the ESR slightly higher compared to other samples. These differences could be related to structural variations of the electrodes that affect the conductivities of the assembly[7]. Furthermore, the R_{ct} value of ACC140_Fe is the smallest, followed by ACC170_Fe and ACC110_Fe, respectively, and thus the ACC140_Fe electrode is expected to present faster ions transfer with a higher diffusion coefficient value (Table 4) estimated from CV using the Randles Sevcik equation[8,57]. A larger ion diffusion coefficient allows easy transport of ions into the electrode material.

$$\frac{i_p}{\sqrt{v}} = 2.69.10^5\, n^{3/2} C_0 A D_0^{1/2} \qquad (2)$$

Where i_p is peak current, v is the scan rate, n is the number of electrons transferred, C_0 is the electrolyte concentration, A is the electrode area and D_0 is the diffusion coefficient.

Lower R_{ct} values associated with a great porosity provide more ion adsorption and consequently enhance the overall electrochemical performance of the electrode[8]. Additionally, the ACC_140 presents the highest diffusion coefficient. These findings agree with the highest value of specific capacitance found for ACC140_Fe (116.8 F g^{-1}).
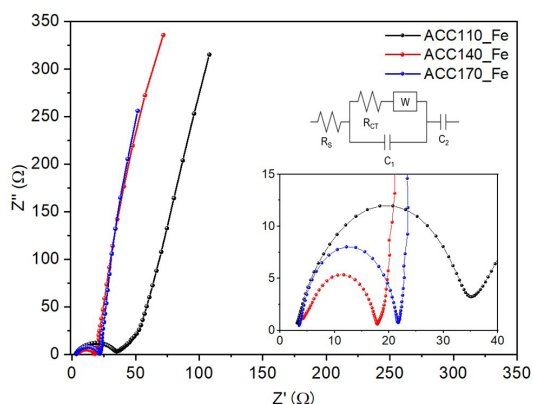

Figure 11. Nyquist plots of ACC110_Fe, ACC140_Fe, and ACC170_Fe. The total equivalent circuit for the plots (inset image).

Table 4. ESR and R_{ct} parameters of flexible electrodes obtained from the Nyquist plots and diffusion coefficients (D) calculated by Equation 1.

SAMPLES	ESR (Ω)	R_{ct} (Ω)	D (cm^2 s^{-1})
ACC110_Fe	3.52	28.4	7.28×10^{-10}
ACC140_Fe	4.57	12.5	1.54×10^{-9}
ACC170_Fe	3.75	17.3	9.72×10^{-10}

4. Conclusions

This work demonstrated the contribution of acidic electrolyte ions in the electrochemical process of flexible electrodes using pre-oxidized carbon cloth as a matrix associated with a simple iron oxide deposition method. The addition of iron to the carbon cloth offered high faradaic contributions, especially when the amount of iron deposited reached 4.08% in the ACC140_Fe electrode. The highest capacitance value of 116.8 F g^{-1} was calculated for the ACC140_Fe sample, and such value is associated with the greater amount of iron, the number of active groups (especially oxygen and iron), the greatest crystallinity of the matrix surface and the developed surface area (557 m^2 g^{-1}). In this electrochemical process, anions have a greater contribution to the final capacitance involving a hybrid pseudocapacitive and double-layer behavior, while the stored energy associated with the H_3O^+ cations exhibit only double-layer characteristics. The successful design of binder-free electrodes through pre-oxidation and spontaneous iron oxide deposition on the carbon matrix boosts the EDLC performance without difficulties or expensive binders to produce carbon-based electrodes.

5. Acknowledgments

6. References

1. Kim BC, Hong JY, Wallace GG, Park HS. Recent progress in flexible electrochemical capacitors: electrode materials, device configuration, and functions. Adv Energy Mater. 2015;5(22):1500959.

2. Simon P, Gogotsi Y. Perspectives for electrochemical capacitors and related devices. Nat Mater. 2020;19(11):1151-63.

3. Najib S, Erdem E. Current progress achieved in novel materials for supercapacitor electrodes: mini review. Nanoscale Adv. 2019;1(8):2817-27.

4. Lin Z, Goikolea E, Balducci A, Naoi K, Taberna PL, Salanne M, et al. Materials for supercapacitors: when Li-ion battery power is not enough. Mater Today. 2018;21(4):419-36.

5. Abdel Maksoud MIA, Fahim RA, Shalan AE, Abd Elkodous M, Olojede SO, Osman AI, et al. Advanced materials and technologies for supercapacitors used in energy conversion and storage: a review. Environ Chem Lett. 2021;19(1):375-439.

6. Martins VL, Torresi RM. Water-in-salt electrolytes for high voltage aqueous electrochemical energy storage devices. Curr Opin Electrochem. 2020;21:62-8.

7. Chakrabarty N, Char M, Krishnamurthy S, Chakraborty AK. Influence of La3+ induced defects on MnO2–carbon nanotube hybrid electrodes for supercapacitors. Mater Adv. 2021;2(1):366-75.

8. Chakrabarty N, Chakraborty AK, Kumar H. Nickel-hydroxide-nanohexagon-based high-performance electrodes for supercapacitors: a systematic investigation on the influence of six different carbon nanostructures. J Phys Chem C. 2019;123(48):29104-15.

9. Chakrabarty N, Dey A, Krishnamurthy S, Chakraborty AK. CeO2/Ce2O3 quantum dot decorated reduced graphene oxide

nanohybrid as electrode for supercapacitor. Appl Surf Sci. 2021;536:147960.

10. Amaral-Labat G, Munhoz MGC, Fonseca BCS, Boss AFN, Almeida-Mattos P, Braghiroli FL, et al. Xerogel-like materials from sustainable sources: properties and electrochemical performances. Energies. 2021;14(23):7977.

11. Grishechko LI, Amaral-Labat G, Szczurek A, Fierro V, Kuznetsov BN, Pizzi A, et al. New tannin–lignin aerogels. Ind Crops Prod. 2013;41(1):347-55.

12. Lamba P, Singh P, Singh P, Singh P, Bharti, Kumar A, et al. Recent advancements in supercapacitors based on different electrode materials: classifications, synthesis methods and comparative performance. J Energy Storage. 2022;48:103871.

13. Terra BM, Andrade DA, Mesquita RN. Characterization of polyacrylonitrile thermal stabilization process for carbon fiber production using intelligent algorithms. Polym Test. 2021;100:107238.

14. Zhong M, Song Y, Li Y, Ma C, Zhai X, Shi J, et al. Effect of reduced graphene oxide on the properties of an activated carbon cloth/polyaniline flexible electrode for supercapacitor application. J Power Sources. 2012;217:6-12.

15. Miller JR, Butler SM. Electrical characteristics of large state-of-the-art electrochemical capacitors. Electrochim Acta. 2019;307:564-72.

16. Muralee Gopi CVV, Vinodh R, Sambasivam S, Obaidat IM, Kim HJ. Recent progress of advanced energy storage materials for flexible and wearable supercapacitor: from design and development to applications. J Energy Storage. 2020;27:101035.

17. Amaral MA Jr, Matsushima JT, Rezende MC, Gonçalves ES, Marcuzzo JS, Baldan MR. Production and characterization of activated carbon fiber from textile PAN fiber. J Aerosp Technol Manag. 2017;9(4):423-30.

18. Rodrigues AC, Munhoz MGC, Pinheiro BS, Batista AF, Amaral-Labat GA, Cuña A, et al. N-activated carbon fiber produced by oxidation process design and its application as supercapacitor electrode. J Porous Mater. 2020;27(1):141-9.

19. Pang S, Lin L, Shen Y, Chen S, Chen W, Tan N, et al. Surface activated commercial carbon cloth as superior electrodes for symmetric supercapacitors. Mater Lett. 2022;315:131985.

20. Tenmyo H, Sugihara R, Ohta A, Uematsu T, Tsuda T, Maruyama J, et al. The capacitor properties of KOH activated porous carbon beads derived from polyacrylonitrile. Bull Chem Soc Jpn. 2019;92(4):832-9.

21. Wang K, Chen Y, Liu Y, Zhang H, Shen Y, Pu Z, et al. Plasma boosted N, P, O co-doped carbon microspheres for high performance Zn ion hybrid supercapacitors. J Alloys Compd. 2022;901:163588.

22. Tiwari S, Bijwe J. Surface treatment of carbon fibers: a review. Procedia Technol. 2014;14:505-12.

23. Xu X, Tian X, Li X, Yang T, He Y, Song Y, et al. The effect of the nitric acid heat treatment time on the electrochemical properties of NiCo2S4/CARBON CLOTH composites as supercapacitor electrode materials. Carbon. 2021;171(3):981.

24. Gopalakrishnan A, Badhulika S. Effect of self-doped heteroatoms on the performance of biomass-derived carbon for supercapacitor applications. J Power Sources. 2020;480:228830.

25. Braghiroli FL, Cuña A, Silva EL, Amaral-Labat G, Lenz e Silva GFB, Bouafif H, et al. The conversion of wood residues, using pilot-scale technologies, into porous activated biochars for supercapacitors. J Porous Mater. 2020;27(2):537-48.

26. He Y, Zhang Y, Li X, Lv Z, Wang X, Liu Z, et al. Capacitive mechanism of oxygen functional groups on carbon surface in supercapacitors. Electrochim Acta. 2018;282:618-25.

27. Hérou S, Crespo Ribadeneyra M, Schlee P, Luo H, Cristian Tanase L, Roßberg C, et al. The impact of having an oxygen-rich microporous surface in carbon electrodes for high-power aqueous supercapacitors. J Energy Chem. 2021;53:36-48.

28. Pramitha A, Raviprakash Y. Recent developments and viable approaches for high-performance supercapacitors using transition metal-based electrode materials. J Energy Storage. 2022;49:104120.

29. Augustyn V, Simon P, Dunn B. Pseudocapacitive oxide materials for high-rate electrochemical energy storage. Energy Environ Sci. 2014;7(5):1597.

30. Mohd Abdah MAA, Azman NHN, Kulandaivalu S, Sulaiman Y. Review of the use of transition-metal-oxide and conducting polymer-based fibers for high-performance supercapacitors. Mater Des. 2020;186:108199.

31. Faraji S, Ani FN. The development supercapacitor from activated carbon by electroless plating: A review. Renew Sustain Energy Rev. 2015;42:823-34.

32. Rodrigues AC, Silva EL, Quirino SF, Cuña A, Marcuzzo JS, Matsushima JT, et al. Ag@Activated carbon felt composite as electrode for supercapacitors and a study of three different aqueous electrolytes. Mater Res. 2018;22(1):1-9.

33. He M, Zheng Y, Du Q. Three-dimensional polypyrrole/MnO$_2$ composite networks deposited on graphite felt as free-standing electrode for supercapacitors. Mater Lett. 2013;104:48-52.

34. Li Y, Li Q, Cao L, Cui X, Yang Y, Xiao P, et al. The impact of morphologies and electrolyte solutions on the supercapacitive behavior for Fe2O3 and the charge storage mechanism. Electrochim Acta. 2015;178:171-8.

35. Ibrahim Abouelamaiem D, Mostazo-López MJ, He G, Patel D, Neville TP, Parkin IP, et al. New insights into the electrochemical behavior of porous carbon electrodes for supercapacitors. J Energy Storage. 2018;19:337-47.

36. Aldama I, Barranco V, Kunowsky M, Ibañez J, Rojo JM. Contribution of cations and anions of aqueous electrolytes to the charge stored at the electric electrolyte/electrode interface of carbon-based supercapacitors. j phys chem c. 2017;121(22):12053-62.

37. Hulicova-Jurcakova D, Seredych M, Jin Y, Lu GQ, Bandosz TJ. Specific anion and cation capacitance in porous carbon blacks. Carbon. 2010;48(6):1767-78.

38. Abbas Q, Gollas B, Presser V. Reduced faradaic contributions and fast charging of nanoporous carbon electrodes in a concentrated sodium nitrate aqueous electrolyte for supercapacitors. Energy Technol. 2019;7(9):1900430.

39. Pohlmann S, Kühnel RS, Centeno TA, Balducci A. The influence of anion-cation combinations on the physicochemical properties of advanced electrolytes for supercapacitors and the capacitance of activated carbons. ChemElectroChem. 2014;1(8):1301-11.

40. Rodrigues AC, Silva EL, Oliveira APS, Matsushima JT, Cuña A, Marcuzzo JS, et al. High-performance supercapacitor electrode based on activated carbon fiber felt/iron oxides. Mater Today Commun. 2019;21:100553.

41. Sadezky A, Muckenhuber H, Grothe H, Niessner R, Pöschl U. Raman microspectroscopy of soot and related carbonaceous materials: spectral analysis and structural information. Carbon. 2005;43(8):1731-42.

42. Fang D, He F, Xie J, Xue L. Calibration of binding energy positions with C1s for XPS results. Journal of Wuhan University of Technology-Mater Sci. 2020;35(4):711-8.

43. Mondal SP, Dhar A, Ray SK, Chakraborty AK. Bonding, vibrational, and electrical characteristics of CdS nanostructures embedded in polyvinyl alcohol matrix. J Appl Phys. 2009;105(8):084309.

44. Brunauer S, Emmett PH, Teller E. Adsorption of gases in multimolecular layers. J Am Chem Soc. 1938;60(2):309-19.

45. Dubinin MM. Fundamentals of the theory of adsorption in micropores of carbon adsorbents: characteristics of their adsorption properties and microporous structures. Carbon. 1989;27(3):457-67.

46. Wang Y, Wu X, Han Y, Li T. Flexible supercapacitor: overview and outlooks. J Energy Storage. 2021;42:103053.

47. Wu K, Fu J, Zhang X, Peng X, Gao B, Chu PK. Three-dimensional flexible carbon electrode for symmetrical supercapacitors. Mater Lett. 2016;185:193-6.

48. Liu M, Yang X, Wu X, Wang X, Li Y, Ma F, et al. Understanding the pore-structure dependence of supercapacitive performance for microporous carbon in aqueous KOH and H_2SO_4 electrolytes. Electrochim Acta. 2022;401:139422.

49. Thommes M, Kaneko K, Neimark AV, Olivier JP, Rodriguez-Reinoso F, Rouquerol J, et al. Physisorption of gases, with special reference to the evaluation of surface area and pore size distribution (IUPAC Technical Report). Pure Appl Chem. 2015;87(9-10):1051-69.

50. Li Q, Jiang R, Dou Y, Wu Z, Huang T, Feng D, et al. Synthesis of mesoporous carbon spheres with a hierarchical pore structure for the electrochemical double-layer capacitor. Carbon. 2011;49(4):1248-57.

51. Grosvenor AP, Kobe BA, Biesinger MC, McIntyre NS. Investigation of multiplet splitting of Fe 2p XPS spectra and bonding in iron compounds. Surf Interface Anal. 2004;36(12):1564-74.

52. Barroso-Bogeat A, Alexandre-Franco M, Fernández-González C, Gómez-Serrano V. Activated carbon surface chemistry: changes upon impregnation with Al(III), Fe(III) and Zn(II)-metal oxide catalyst precursors from $NO3^-$ aqueous solutions. Arab J Chem. 2019;12(8):3963-76.

53. Li ZQ, Lu CJ, Xia ZP, Zhou Y, Luo Z. X-ray diffraction patterns of graphite and turbostratic carbon. Carbon. 2007;45(8):1686-95.

54. Ferrari AC, Robertson J. Interpretation of Raman spectra of disordered and amorphous carbon. Surf Coat Tech. 2006;232(4):1-14.

55. Eliad L, Salitra G, Soffer A, Aurbach D. Ion sieving effects in the electrical double layer of porous carbon electrodes: estimating effective ion size in electrolytic solutions. J Phys Chem B. 2001;105(29):6880-7.

56. Pang J, Zhang W, Zhang H, Zhang J, Zhang H, Cao G, et al. Sustainable nitrogen-containing hierarchical porous carbon spheres derived from sodium lignosulfonate for high-performance supercapacitors. Carbon. 2018;132:280-93.

57. Vangapally N, v KK, Kumar A, Martha SK. Charge storage behavior of sugar derived carbon/MnO_2 composite electrode material for high-performance supercapacitors. J Alloys Compd. 2022;893:162232.